J. Fluid Mech. (2013), *vol.* 714, *pp.* 644–670. © Cambridge University Press 2013
doi:10.1017/jfm.2012.519

Thermocapillary flow regimes and instability caused by a gas stream along the interface

V. Shevtsova†, Y. A. Gaponenko and A. Nepomnyashchy

Microgravity Research Center, Université Libre de Bruxelles, CP-165/62 av. F. D. Roosevelt, 50, B-1050 Brussels, Belgium

(Received 25 May 2012; revised 22 August 2012; accepted 15 October 2012)

We present the results of a numerical study of the thermocapillary (Marangoni) convection in a liquid bridge of $Pr = 12$ (n-decane) and $Pr = 68$ (5 cSt silicone oil) when the interface is subjected to an axial gas stream. The gas flow is co- or counter-directed with respect to the Marangoni flow. In the case when the gas stream comes from the cold side, it cools down the interface to a temperature lower than that of the liquid beneath and in a certain region of the parameter space that cooling causes an instability due to a temperature difference in the direction perpendicular to the interface. The disturbances are swept by the thermocapillary flow to the cold side, which leads to the appearance of axisymmetric waves propagating in the axial direction from the hot to cold side. The mechanism of this new two-dimensional oscillatory instability is similar to that of the Pearson's instability of the rest state in a thin layer heated from below (Pearson, *J. Fluid Mech.*, vol. 4, 1958, p. 489), and it appears at the value of the transverse Marangoni number $Ma_{\perp}^{cr} \approx 39$–$44$ lower than that of the Pearson's instability in a horizontal layer ($48 < Ma_{\perp}^{cr} < 80$, depending on the Biot number). The generality of the instability mechanism indicates that it is not limited to cylindrical geometry and might be observed in a liquid layer with cold gas stream.

Key words: interfacial flows (free surface), liquid bridges, multiphase and particle-laden flows

1. Introduction

The investigation of instabilities induced by the thermocapillary effect has been initiated by Pearson (1958) who has shown that the temperature dependence of the free surface tension by itself is capable of producing an instability in a fluid layer heated from below. The stability of thermocapillary flows generated by a temperature gradient directed along the liquid surface has been studied extensively in the case of a thin liquid layer, see Davis (1987). Another important class of thermocapillary flows, which is connected with the floating-zone crystal growth technique, is that of flows in a cylindrical liquid bridge. The stability of a parallel flow in an infinite cylindrical column has been studied by Xu & Davis (1984) who revealed the appearance of two-dimensional and three-dimensional hydrothermal waves similar to those observed in a thin liquid layer (on the relation between instabilities in both geometrical configurations, see Kawamura & Tagaya (2007)). In the more realistic

† Email address for correspondence: vshev@ulb.ac.be

https://doi.org/10.1017/jfm.2012.519 Published online by Cambridge University Press

case of a finite cylindrical zone, a number of instability modes with different azimuthal wavenumbers have been found (for reviews see Kuhlmann (1999) and Lappa (2010) and for numerical and experimental benchmarks see Shevtsova (2005) and Shevtsova *et al.* (2011)). In the above-mentioned works, the phenomena in the gas surrounding the liquid bridge have been ignored.

Recently, the effect of ambient gas on the stability of the flow inside a liquid bridge has become an object of investigation. Experiments by Shevtsova, Mialdun & Mojahed (2005) and Mialdun & Shevtsova (2006) in shielded and non-shielded liquid bridges clearly showed a dependence of the critical parameters of instability (critical temperature difference and frequency of oscillations) on the surrounding conditions and the temperature of shielding. Kamotani's group performed experiments (Kamotani *et al.* 2003; Wang, Kamotani & Yoda 2007) placing a liquid bridge in an oven at different temperatures that demonstrated a strong dependence of critical parameters on the ambient air temperature. In some of their experiments, e.g. Kamotani *et al.* (2003), a thin plastic plate was placed at a certain height around a liquid column without touching the free surface. Depending on the location of the plate, the stability of the flow varied strongly due to the alteration of heat transfer near the free surface. Irikira *et al.* (2005) investigated experimentally and numerically in which way the volume of gas space around a liquid bridge affects the onset of its instability. The volume of the ambient air region was varied by placing two thin discs perpendicular to the liquid bridge. Somewhat similar configurations were studied numerically and experimentally by Tiwari & Nishino (2007, 2010).

The number of publications considering the flows both in the liquid bridge and in the surrounding fluid is still rather small. Herrada *et al.* (2011) and Gaponenko, Mialdun & Shevtsova (2012) have recently examined isothermal gas–liquid flows in an annulus for physically realistic systems. The former study was focused on the characteristics of the liquid flow entrained by gas and the latter was focused on the interface deformation.

Experiments in a 2 cSt silicone oil/air system by Ueno, Kawazoe & Enomoto (2010) have shown that the stability of a thermocapillary flow in a liquid bridge is strongly affected by the direction of the gas stream. The gas was blown at room temperature and its velocity was rather low, $Re^g \leqslant 100$. The authors reported that for the considered geometry the gas pumped in the direction of the thermocapillary flow plays a stabilizing role while the gas pumped from the cold side destabilizes the flow.

The thermocapillary flows in an infinite liquid bridge surrounded by an annular channel of gas with the axial temperature gradient have been investigated by Ryzhkov & Shevtsova (2012) using linear stability analysis. The authors reported that gas pumping in the same direction with respect to the thermocapillary motion on the interface has a destabilizing effect on the system. Gas pumping in the opposite direction can be stabilizing or destabilizing depending on the gas flow rate.

This study is connected to the microgravity experiment JEREMI (Japanese European Research Experiment on Marangoni Instabilities) where the use of a forced coaxial gas stream is proposed to control the hydrothermal instabilities in liquid bridges. The use of the silicone oil is foreseen during the experiments on the International Space Station (ISS). Correspondingly, the subject of this study is the flow in viscous fluids, such as silicone oil ($Pr = 68$) and n-decane ($Pr = 12$), driven by thermocapillary force and co- and counter- current gas flow in zero gravity conditions. Here we present, to the best of the authors' knowledge, one of the first numerical studies of a two-phase flow in a non-isothermal liquid bridge.

https://doi.org/10.1017/jfm.2012.519 Published online by Cambridge University Press

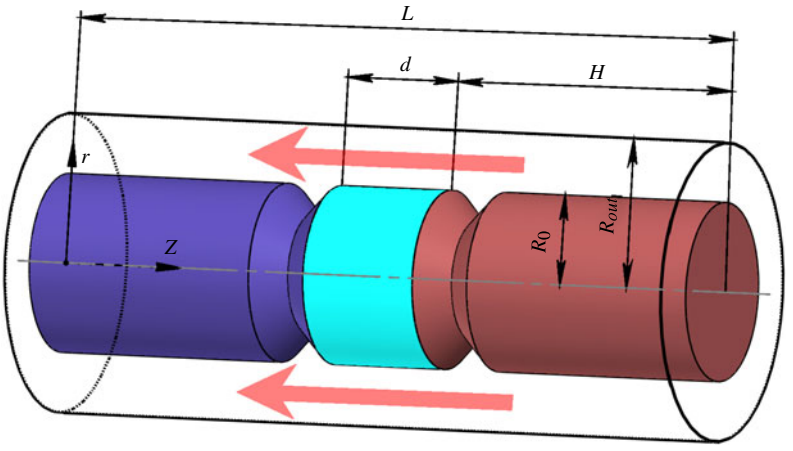


FIGURE 1. (Colour online) Geometry and scales used in numerical simulations. Gas may enter from the left- or right-hand side.

In § 2, we formulate the mathematical model, and discuss the numerical approach and the code validation. Section 3 is devoted to the description of the results of numerical simulations. The stationary flow regimes for $Pr = 68$ are considered in the first part of the section and the oscillatory regimes, stability diagrams and heat fluxes for $Pr = 12$ and $Pr = 68$ are analysed in the second part. Finally, we discuss the mechanism of instability at the end of § 3. Concluding remarks are presented in § 4.

2. Numerical modelling

2.1. *Problem formulation*

We consider the system consisting of two coaxial cylinders, see the geometry and notation in figure 1. The outer cylinder is a solid tube of radius R_{out}. The inner cylinder consists of two solid rods of radius R_0 and a liquid bridge between them, which is kept in its position by the surface tension force. Gas of a constant flow rate Q_{in} enters from the right or left and flows through the annular duct of a size $(R_{out} - R_0)$. The solid rods are rather long; the distance from the tube inlet is H while $H/(R_{out} - R_0) = 10$. This provides a fully developed flow in the gas, i.e. parabolic velocity profile unchanging in the flow direction, before reaching the liquid zone. The flow structure at the entrance zone was analysed earlier by Gaponenko, Ryzhkov & Shevtsova (2010).

Upon reaching the liquid zone, a forced gas flow interplays with a liquid thermocapillary flow, which is present when the temperature difference is imposed between the rods. After passing the liquid zone of the length d, the gas continues to move through the annular duct over the distance H up to the tube outlet. The total length of the tube is $L = 2H + d$. The geometrical dimensions are given in table 1 and they correspond to the geometry of the new set-up at the Microgravity Research Center (MRC), which is under development.

In this study the gravity is not taken into account and the liquid bridge is placed horizontally in figure 1. In the case of a vertical configuration the system is usually heated from above. The temperature of the lower rod is either kept constant or diminished to maintain the mean temperature at a constant level in the system.

https://doi.org/10.1017/jfm.2012.519 Published online by Cambridge University Press

R_{out} 10^{-3} m	R_0 10^{-3} m	D_h 10^{-3} m	H 10^{-3} m	d 10^{-3} m	L 10^{-3} m
5	3	4	20	6	46

TABLE 1. Geometrical scales used in the calculations, unless otherwise stated.

Fluid	μ (Pa s)	χ ($m^2\ s^{-1}$)	k (W m^{-1} K^{-1})	ρ (kg m^{-3})	$\sigma_T = -d\sigma/dT$ (N m^{-1} K^{-1})	Pr
Silicone oil	4.56×10^{-3}	7.31×10^{-8}	0.11	912	6.37×10^{-5}	68
n-decane	0.75×10^{-3}	8.45×10^{-8}	0.135	730	1.18×10^{-4}	12.2
Air	17.9×10^{-6}	1.9×10^{-5}	0.025	1.225		0.713

TABLE 2. Physical properties of silicone oil 5 cSt, *n*-decane and air.

To prevent the liquid from creeping over the edges of the rods, they have to be coated with an anti-wetting barrier, which depends on the liquid and on the material of the rods. In the experiments with large ΔT the use of an anti-wetting barrier may be not sufficient for the prevention of creeping. In that case, sharp edges are made in both rods, see Masud, Kamotani & Ostrach (1997). The size of triangle grooves is taken to be equal to 0.5 mm in horizontal and vertical directions, see figure 1, and they are captured by the numerical code. The physical properties of the fluids are given in table 2. The gas is assumed to be incompressible in consistency with the low pressure drop between the tube ends. The thermocapillary flow arises in the liquid for arbitrary small temperature difference ΔT between the supporting rods.

The dynamics of the system in the geometry of figure 1 is described by the momentum, continuity and heat transfer equations for an incompressible Newtonian fluids which are written for gas (^{g}) and liquid (^{l}):

$$\partial_t \boldsymbol{V}^g + (\boldsymbol{V}^g \cdot \boldsymbol{\nabla})\boldsymbol{V}^g = -\frac{1}{\rho^g}\boldsymbol{\nabla} P^g + \frac{\mu^g}{\rho^g}\nabla^2 \boldsymbol{V}^g, \quad \boldsymbol{\nabla} \cdot \boldsymbol{V}^g = 0, \tag{2.1a}$$

$$\partial_t T^g + \boldsymbol{V}^g \cdot \boldsymbol{\nabla} T^g = \chi^g \nabla^2 T^g, \tag{2.1b}$$

$$\partial_t \boldsymbol{V}^l + (\boldsymbol{V}^l \cdot \boldsymbol{\nabla})\boldsymbol{V}^l = -\frac{1}{\rho^l}\boldsymbol{\nabla} P^l + \frac{\mu^l}{\rho^l}\nabla^2 \boldsymbol{V}^l, \quad \boldsymbol{\nabla} \cdot \boldsymbol{V}^l = 0, \tag{2.1c}$$

$$\partial_t T^l + \boldsymbol{V}^l \cdot \boldsymbol{\nabla} T^l = \chi^l \nabla^2 T^l, \tag{2.1d}$$

where T is the temperature, μ is the dynamic viscosity, χ is the thermal diffusivity and ρ is the density. The numerical model in the current work is limited to an axisymmetrical configuration, where the velocity $\boldsymbol{V} = [V, U]$ includes the radial V and axial U components.

The gas/liquid interface is assumed non-deformed in the considered range of the aspect ratios, $\Gamma \leqslant 2$. This assumption is supported by recent experimental studies by Matsunaga *et al.* (2012). The experiments were performed in the isothermal case in the geometry of interest and for the liquid with $Pr = 68$. The measurements have shown

https://doi.org/10.1017/jfm.2012.519 Published online by Cambridge University Press

that the interface deformation by the gas stream is scaled by the capillary number which defined as

$$Ca_{shear} = \frac{\nu_g \rho_g U_0^g}{\sigma} \frac{R_{out} - R_0}{R_0} \left(\frac{d}{R_0} \right)^2 \tilde{f}(V) \tag{2.2}$$

where $\tilde{f}(V)$ is a function of the volume ratio. This gives the interface deformation by the gas stream ($Re^g \leqslant 550$) of a few micrometres. In the non-isothermal case, experimental (Montanero, Ferrera & Shevtsova 2008) and numerical (Shevtsova *et al.* 2008) studies have reported that the interface deformation caused by thermocapillary steady flow is proportional to the capillary number, which defined is as

$$Ca_{Ma} = \sigma_T \Delta T / \sigma. \tag{2.3}$$

This leads to a similar value of the interface deformation $\sim$20 μm. So, for the parameters of interest the interface deformation is slightly smaller than one step size of the computational spatial grid. The boundary conditions on the liquid–gas interface $r = R_0$ are:

(*a*) a balance of viscous and thermocapillary stresses

$$\mu^l \partial_r U^l + \sigma_T \partial_z T^l = \mu^g \partial_r U^g, \tag{2.4}$$

where the surface tension σ is a linear function of temperature

$$\sigma(T) = \sigma(T_0) - \sigma_T (T - T_0), \quad \sigma_T \equiv -\partial_T \sigma = \text{const}, \tag{2.5}$$

and T_0 is the reference temperature equal to the mean temperature of the system $T_0 = (T_{cold} + T_{hot})/2$;

(*b*) the axial velocities of the liquid and gas are equal; radial velocities vanish (interface deformation is neglected)

$$U^l = U^g, \quad V^l = V^g = 0; \tag{2.6}$$

(*c*) the heat fluxes in the liquid and gas and the temperatures of the liquid and gas are equal; here k is the thermal conductivity

$$k^l \partial_r T^l = k^g \partial_r T^g, \quad T^l = T^g. \tag{2.7}$$

On the liquid bridge axis $r = 0$ the symmetry conditions are imposed:

$$\partial_r U^l = 0, \quad V^l = 0, \quad \partial_r T^l = 0. \tag{2.8}$$

No-slip conditions are imposed on the wall of the external tube $r = R_{out}$:

$$U^g = 0, \quad V^g = 0. \tag{2.9}$$

The temperature of the external wall can be considered as a control parameter, but it is taken equal to the mean temperature of the system if it is not stated otherwise:

$$T^g(r = R_{out}) = T_0. \tag{2.10}$$

No-slip conditions and constant temperatures are also imposed on the supporting rods:

$$\text{on the left rod } 0 \leqslant z \leqslant H, \quad U^g = V^g = 0, \quad T^g = T_{cold}; \tag{2.11a}$$

$$\text{on the right rod } H + d \leqslant z \leqslant L, \quad U^g = V^g = 0, \quad T^g = T_{hot}. \tag{2.11b}$$

https://doi.org/10.1017/jfm.2012.519 Published online by Cambridge University Press

The inlet conditions at $z = 0$ or $z = L$ (depending on which side the gas enters into the duct), $R_0 < r < R_{out}$ are

$$U^g = U_0^g = \text{const}, \quad V^g = 0, \quad T^g = T_{in}, \tag{2.12}$$

alternatively, a constant flow rate, calculated as $Q_{in} = U_0\pi(R_{out}^2 - R_0^2)$, can be fixed.

Let us discuss the outlet conditions imposed at $z = 0$ (in the case where the gas enters from the right), $R_0 < r < R_{out}$. The flow velocity and pressure at the outlet are not known prior to the solution of the flow problem. The 'soft' conditions applied at outflow boundaries when the velocity profiles are physically appropriate for fully developed flows are

$$\partial_z U^g = 0, \quad \partial_z V^g = 0, \quad \partial_z T^g = 0. \tag{2.13}$$

The question of whether these conditions allow perturbations to penetrate back inside the tube have been investigated previously by Gaponenko *et al.* (2010). The simulations were performed with an extended outlet part to analyse artificial boundary effects. The results for the length $0 < z < L$, and an extended length $0 < z < L + H/2$ appeared to be rather similar.

As an initial state, a zero velocity field and the mean temperature have been chosen.

The system is multi-parametric and the major control parameters are the Marangoni number Ma, Prandtl number Pr, Reynolds number of the gas Re^g, viscosity ratio $\tilde{\mu}$, thermal conductivity ratio $\tilde{k}$ and aspect ratio Γ:

$$Pr = \frac{\mu}{\rho\chi^l}, \quad Re^g = \frac{\rho^g U_0^g D_h}{\mu^g}, \quad Ma = \frac{\sigma_T \Delta T\, \mathrm{d}}{\mu^l \chi^l}, \quad \tilde{\mu} = \frac{\mu^l}{\mu^g}, \quad \tilde{k} = \frac{k^l}{k^g}, \quad \Gamma = \frac{\mathrm{d}}{R_0}, \tag{2.14}$$

where $\nu = \mu/\rho$ is the kinematic viscosity and $D_h = 2(R_{out} - R_0)$ is the hydraulic diameter which is a typical length scale in an annulus. For the geometry and fluid properties listed in tables 1 and 2 the dimensionless parameters can be written in a way convenient for comparison (U_0^g is in (m s^{-1}))

$$Pr^g = 0.75, \quad Re^g = 273U_0^g, \quad Ma_{Pr=68} = 573\Gamma\Delta T, \quad Ma_{Pr=12} = 5572\Gamma\Delta T. \tag{2.15}$$

It is important to stress that a very large number of parameters appear in (2.1*b*)–(2.13) and it is not feasible to carry out a general parametric study. For this reason, we shall restrict our analysis to two liquids ($Pr^l = 12, 68$) and two aspect ratios ($\Gamma = 1, 2$).

2.2. *Heat transfer and Biot number*

To define heat transfer through the interface, the heat flux can be associated with the Biot number. The local heat flux through the unit of the free surface area will be determined from the calculations as

$$\tilde{q}(z) = -k^l \partial_r T^l (r = R_0) \tag{2.16}$$

while the averaged heat flux is $\tilde{q}_{av} = 1/\mathrm{d} \int \tilde{q}(z)\, \mathrm{d}z$. Then the net flux through the entire interface is

$$Q = S \times \frac{1}{d} \int \tilde{q}(z)\, \mathrm{d}z = 2\pi R_0\, \mathrm{d}\tilde{q}_{av}. \tag{2.17}$$

When only the flow in the liquid phase is considered, the heat flux through the unit of the free surface is usually written as

$$-k^l\, \mathrm{d}T/\mathrm{d}r = h(T_s - T_{amb}), \tag{2.18}$$

https://doi.org/10.1017/jfm.2012.519 Published online by Cambridge University Press

where h is the heat transfer coefficient to the ambient air, k^l is the thermal conductivity of the liquid and T_s and T_{amb} are the temperatures of the interface and ambient air. Let us define the Biot number as $Bi = hR_0/k^l$, then the entire heat flux from (2.18) can be written as

$$Q = 2\pi R_0 dh \cdot \frac{1}{d}\int (T_s - T_{amb})\,\mathrm{d}z \approx Bi \times 2\pi k^l \delta T \quad \text{where } \delta T = (T_s - T_{amb}). \tag{2.19}$$

Finally, the Biot number can be determined by substituting (2.19) into (2.18)

$$Bi = \frac{R_0}{k^l \Delta T}\frac{\Delta T}{\delta T}\tilde{q}_{av} = \frac{\Delta T}{\delta T} q_{av}. \tag{2.20}$$

The non-dimensional heat flux q_{av} is scaled as $q_{av} = R_0/k^l \Delta T \tilde{q}_{av}$. In the discussion below the local q and averaged q_{av} non-dimensional heat flux will be used. The heat flux q is positive when the liquid locally loses heat and negative for heat gain. Correspondingly, q_{av} are positive (negative) when the liquid integrally loses (gains) heat.

The quantity $\delta T = (T_s - T_{amb})$ plays an important role in the determination of the Biot number. Kamotani *et al.* (2003), Wang *et al.* (2007) and Simic-Stefani, Kawaji & Yoda (2006) considered in their estimations that the difference between interface and ambient temperature (δT) is equal to the temperature between rods, i.e. $\delta T = \Delta T$. This Biot value is under-evaluated as in general the major part on the interface has temperature $T_s \cong T_{cold} + 0.7\Delta T$ and more precise estimation should assume at least $\delta T \approx 0.5\Delta T$ or less.

2.3. *Numerical solution and code verification*

The commercial solver FLUENT v.6.3 was used for solving governing equations (2.1*b*)–(2.13). The problem was solved using dimensional variables in two domains for each phase separately with taking into account the boundary conditions at the interface, (2.4)–(2.7). In order to satisfy the conditions at the interface very accurately, an iterative procedure was used according to the approach of Lombardi, De Angelos & Banerjee (1986). The iterative procedure is accomplished by prescribing the surface velocity and temperature and then calculating the shear stress and heat flux at the interface on one side. Using this shear stress and heat flux, the interfacial velocity field could then be calculated on the other side. At each time step the procedure is repeated until equal fields are obtained on both sides. By means of a user-defined function the procedure is implemented with the shear stress and heat flux continuity boundary condition on the liquid side (shear stress known at the interface) and the velocity and temperature continuity boundary condition on the gas side (velocity and temperature known at the interface).

A check on the validity of the calculations has been done by reducing by a factor of two the time step used in the runs (0.001 s) to determine whether there are any effects on the flow organization. The check indicated negligible changes for the time steps used in the calculations presented here. At present there are no validation data for the problem of liquid–gas dynamic interaction, therefore the code validation procedure was performed in a gas and a liquid zone separately. The results of the comparison of numerical and analytical solutions for a gas flow may be found in Gaponenko *et al.* (2010). To validate the numerical model in the liquid bridge volume quantitative comparisons were made with the simulation results presented in Lappa, Savino & Monti (2001). For the test problem an axisymmetric flow was considered with parameters $Pr = 10$, $Ma = 1000$ and $\Gamma = 1$ for different meshes. As the gas flow

https://doi.org/10.1017/jfm.2012.519 Published online by Cambridge University Press

Grid size	$\Delta r = \Delta z$ (m)	u at $r = 0.25R_0$	u at $r = 0.5R_0$	u at $r = R_0$
40×40	Lappa *et al.* (2001) or $\Delta r = 7.5 \times 10^{-5}$	14.44	16.605	−43.77
60×60	or $\Delta r = 5 \times 10^{-5}$	13.370	16.557	−41.787
80×80	or $\Delta r = 3.75 \times 10^{-5}$	13.307	16.487	−42.470
100×100	or $\Delta r = 3 \times 10^{-5}$	13.294	16.470	−42.586
150×150	or $\Delta r = 2 \times 10^{-5}$	13.284	16.462	−42.646

TABLE 3. Dimensionless axial velocity in the cross-section ($z = H + d/2$) of a liquid bridge at different radial positions as a function of grid spacing.

was not taken into account, the boundary conditions at the interface were modified:

$$\mu^l \partial_r U^l + \sigma_T \partial_z T^l = 0, \quad V^l = 0, \quad \partial_r T^l = 0. \tag{2.21}$$

The results of the test problem calculation as well as the grid refinement study are shown in table 3. An axial velocity distribution in the cross-section of a liquid bridge was considered for the code validation and mesh refinement check. According to these results the square grid 80×80 or spatial spacing $\Delta r = \Delta z = 3.75 \times 10^{-5}$ m were used in the liquid phase. However, for large values of Ma and Re^g the control calculations were performed on a double grid.

Computations in multi-domains require a complicated computational mesh, which was generated by the commercial code GAMBIT. A square grid with spatial steps Δr and Δz was used for the calculation only in the liquid bridge as the most important part of computational domain (see figure 2). A non-uniform grid was chosen for a space discretization of the gas flow except the area near the grooves where a triangle grid was used. The edge mesh has a stretch factor of 1.05 and 75 nodes in any direction. Note that the smallest cells lie in the region of the liquid zone and around the grooves. In that region the smallest mesh cell size is 2×10^{-5} m.

3. Numerical results

3.1. *Stationary flows*

3.1.1. *No forced gas stream*

In the absence of a gas stream the flow is induced by thermocapillary stresses due to the temperature gradient along the interface. The liquid moves from the hot to the cold side along the interface and the flow pattern consists of one vortex with a centre shifted to the hot side. In this section we compare two kinds of flows: (i) the flows in a single-phase liquid bridge with boundary conditions as in (2.21); and (ii) two-phase flows in a system which consists of a liquid bridge and a passive gas, $U_0^g = 0$. The flow in the gas is driven by the liquid shear. The flow structure consists of two small recirculation regions with the same direction of circulation (cat's eyes) embedded in a globally circulating flow over the whole duct region (see figure 3*b*). These recirculation regions correlate with two peaks on the interface velocity profile shown in figure 4(*b*).

The unidirectional flow near the free surface drives the hot liquid along the interface towards the cold region, see figure 3(*b*). Here we would like to draw the attention to the following point: the presence of ambient gas at the mean temperature, which is natural for any experiment, diminishes the interface temperature. The temperature fields in both phases are shown in figure 3(*a*) and the temperature profiles across the

https://doi.org/10.1017/jfm.2012.519 Published online by Cambridge University Press

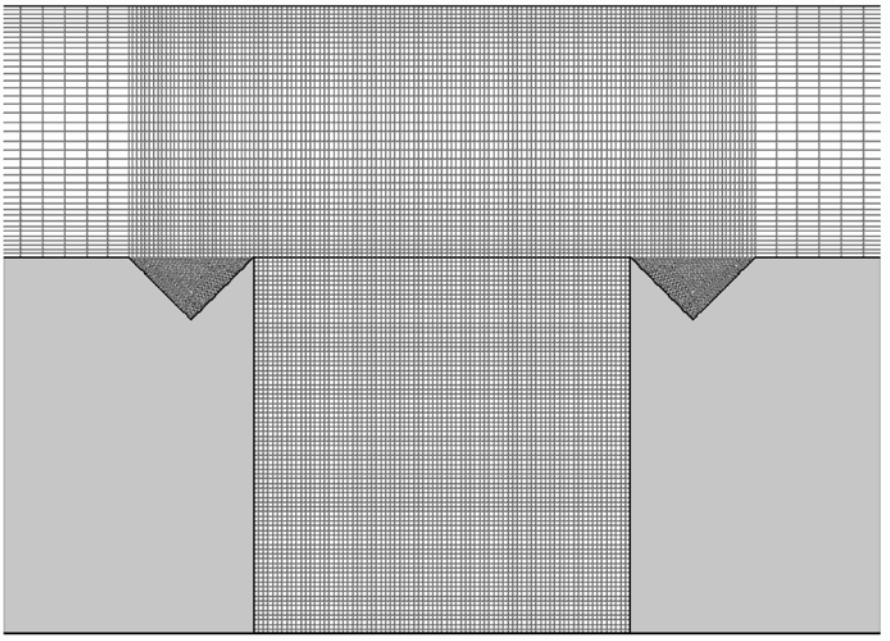


FIGURE 2. Computational mesh.

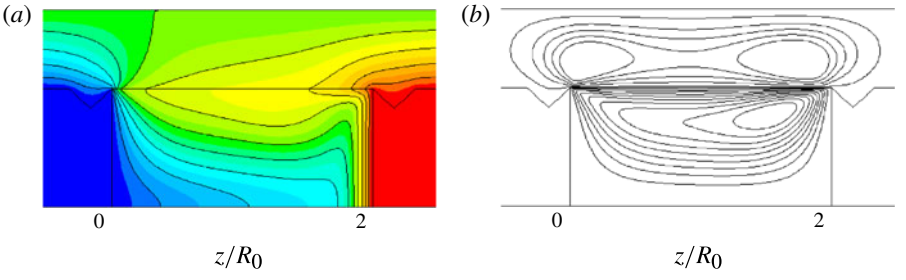


FIGURE 3. (Colour online) Temperature field and isolines of stream functions in two phases without forced gas motion, $Pr = 68$, $\Delta T = 5$ K, $U_0^g = 0$ m s^{-1}, $T^g = T_0$ and $\Gamma = 2$.

interface for these cases are shown below in figure 9(*b*) by dashed (no gas) and solid '1' (with gas) curves, respectively.

To analyse the effect of a heat gain/loss we performed simulations for the cases when the temperature of ambient gas is equal to the mean temperature of the system and with either a cold or hot rod. By keeping the wall of an external tube at the temperature of the gas the system becomes similar to that of the Kamotani group (Wang *et al.* 2007) who performed experiments placing the liquid bridge in the oven with controlled temperature. They studied the effect of heat gain in the presence of buoyancy force and concluded that the flow becomes oscillatory as a result of interaction between buoyancy and thermocapillarity. In the present model, the buoyancy is absent but the heat transfer also plays an important role. For the cases mentioned above the local heat flux q is shown in figure 4(*a*) and velocity profiles in

https://doi.org/10.1017/jfm.2012.519 Published online by Cambridge University Press

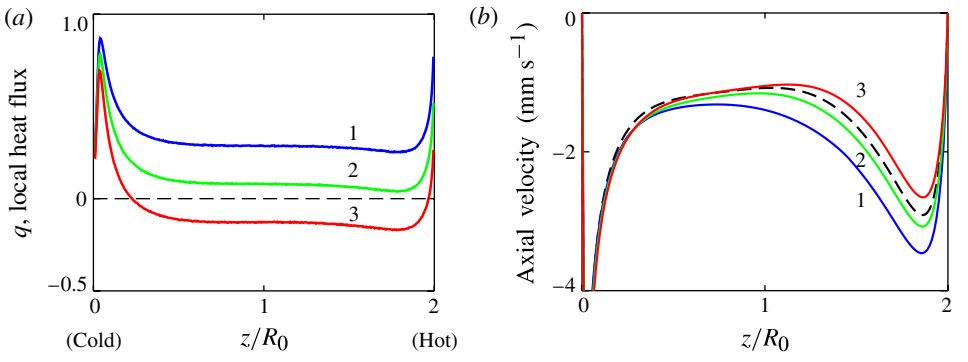


FIGURE 4. (Colour online) The local heat flux (*a*) and the velocity (*b*) along the free surface when $Pr = 68$, $\Delta T = 5$ K and $\Gamma = 2$. Curves 1, 2 and 3 correspond to the passive gas with temperature T_{cold}, T_0 and T_{hot}, respectively. Temperature of the external tube is equal to the temperature of the gas. The dashed curve in (*b*) corresponds to the case when ambient gas is not considered.

figure 4(*b*) where curves 1, 2 and 3 correspond to the ambient gas at the temperatures T_{cold}, T_0 and T_{hot}, respectively. It follows from the graph that the heat flux in cases 1 and 2 is positive (heat loss) while in case 3 it is negative (heat gain). The mean fluxes for the cases 1–3 are $q_{av} = 0.32, 0.12$ and -0.08, respectively.

Correspondingly, the presence of ambient gas changes the temperature gradients along the interface which is crucial for the driving force. Two peaks on the velocity profile are induced by large local temperature gradients near hot and cold rods that accelerate/decelerate the liquid flow due to thermocapillary stresses, see the dashed line in figure 4(*b*). The modification of the temperature profile by gas leads to the adjustment of the velocity on the interface with more pronounced changes near the hot side. The peak velocity on the cold side is too large to be shown in the graph scale, it ranges from -5.0 to -5.9 mm s^{-1} for curves 1–3. Only in the case of hot gas does the flow on the free surface slow down with respect to the adiabatic case. Surrounding gas at the mean or colder temperature accelerates the flow. We may conclude that the heat loss, $q_{av} > 0$, enhances the flow on the interface (curves 1 and 2 in figure 4*b*) while the heat gain slows down the flow (curve 3). Our calculations show that this trend is valid for the aspect ratio $\Gamma = 1$ and other values of ΔT.

The calculations with grooves demonstrate the increase of overshooting on the curves of the heat fluxes near the solid walls because of a slightly non-uniform temperature near the edges of the rods.

3.1.2. *Gas stream co-directed with Marangoni force*

Here we consider the case where the gas enters from the right-hand side having temperature at the inlet $T_0^g = T_0$. The external tube temperature is also equal to the mean temperature T_0. In the presence of a gas stream the Marangoni flow is affected not only by the temperature of the ambient gas but also by the viscous shear stresses. When the gas stream is co-directed with Marangoni flow, it moves along the hot rod and the gas warms up inside a layer adjacent to the rod. The thickness δ of the preheated layer can be estimated from the balance between the time interval, when the gas is moving along the hot rod, $\sim H/U_0^g$, and the thermal time, δ^2/χ^g. Thus,

$$\delta \sim \sqrt{H\chi^g/U_0^g}. \tag{3.1}$$

https://doi.org/10.1017/jfm.2012.519 Published online by Cambridge University Press

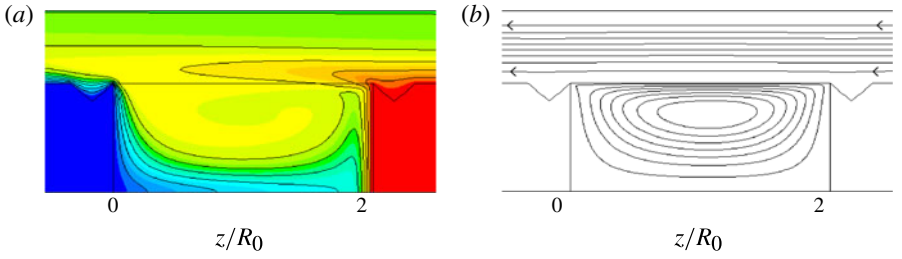


FIGURE 5. (Colour online) Isolines of the temperature field and stream functions in two phases when the gas stream is co-directed with Marangoni force, $Pr = 68$, $\Delta T = 5$ K, $U_g^0 = -1.0$ m s^{-1} ($|Re^g| = 273$) and $\Gamma = 2$.

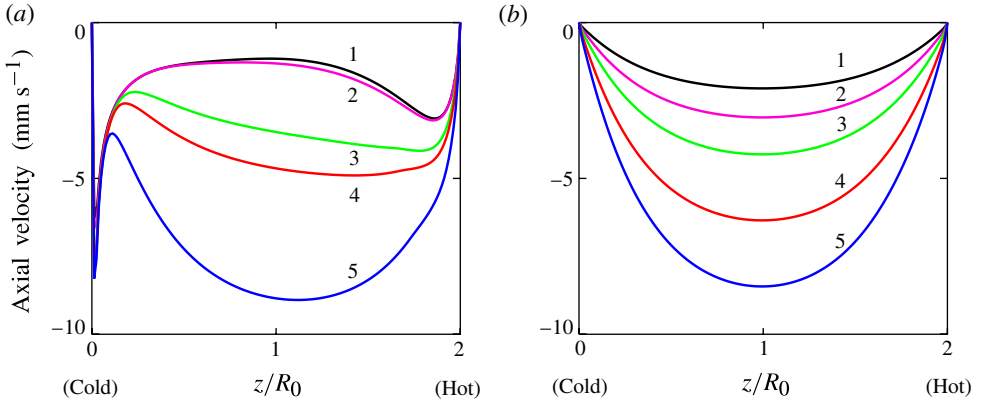


FIGURE 6. (Colour online) Distribution of velocity along the free surface (*a*) when $\Delta T = 5$ K and (*b*) shear-driven flow (isothermal case). Curves 1–5 in graph (*a*) correspond to the gas velocities $U_0^g = 0, -0.05, -0.36, -0.5, -1$ m s^{-1}, respectively. Curves 1–4 in graph (*b*) correspond to the gas velocities $U_0^g = -0.25, -0.36, -0.5, -0.75, -1$ m s^{-1}, respectively.

The thickness δ depends on the gas velocity but in any case there is a layer where the temperature is close to T_{hot}. The isolines of the temperature field are shown in figure 5(*a*). The liquid interface is colder than the gas and it gains heat. As was discussed in the previous paragraph, the heat gain slightly decelerates the flow. On the other hand the co-directed viscous shear stress tends to pull the liquid along with it and accelerates the flow. Thus, at a very low gas velocity the flow in the liquid slows down because of the heat gain and for a larger gas velocity the flow speeds up due to the shear stresses. Our calculations show that the interface velocity regains a value similar to that in the case of a passive gas at $T_0^g = T_0$ when the gas velocity is about $U_0^g = -0.05$ m s^{-1}; compare curves 1 and 2 in figure 6(*a*). The noticeable modifications in the velocity profile start when shear and Marangoni contributions to the velocity have the same order of magnitude, see curve 3 in figure 6(*a*), because the velocity distributions on the interface have different shapes depending on the driving force. In the case of a Marangoni-driven flow there are two pronounced peaks near the solid walls (curve 1 in figure 6*a*) while the shear-driven velocity reaches a maximum in the middle of the liquid zone as shown in figure 6(*b*), see also Gaponenko *et al.* (2010) and Gaponenko, Mialdun & Shevtsova (2011). The distinct

https://doi.org/10.1017/jfm.2012.519 Published online by Cambridge University Press

peak of the interface velocity near the hot corner associated with a Marangoni flow disappears at $U_0^g = -0.36$ m s^{-1} ($Re^g \sim 100$). For larger U_0^g the flow is dominated by shear stresses which follows from the comparison of curves 5 (figure 6*a*) and 4 (figure 6*b*) attributed to the same gas speed $U_0^g = -1$ m s^{-1}. For all gas speeds the flow pattern is one vortex but its centre is blown by gas from the hot corner (figure 3) to the central part (figure 5*b*).

The results obtained by Gaponenko *et al.* (2012) for shear-driven flows indicate that for large viscosity ratios $\mu^l/\mu^g > 50$ the free surface velocity of liquid depends linearly on the gas velocity

$$\max |U^l|_{shear} \sim \alpha^g \frac{R_0}{(R_{out} - R_0)} \Gamma \frac{\mu^g}{\mu^l} U_0^g, \tag{3.2}$$

where the scaling factor $\alpha^g = 0.73$ is obtained empirically. It follows from (3.2) that for $U_0^g = 0.36$ m s^{-1} the shear-driven velocity is $\sim 3.08 \times 10^{-3}$ m s^{-1}. It matches with the peak velocity in curve 1 (figure 6*a*) caused by the Marangoni force, which is $\max |U^l_{Ma}| \sim 3.08 \times 10^{-3}$ m s^{-1}. Correspondingly, curve 3 in figure 6(*a*) reflects the results of the comparable contributions of both stresses.

For all considered cases the flow field consists of one recirculation cell, see figure 5(*b*). The temperature of the free surface changes in an agreement with the dynamics described above. Figure 5(*a*) shows that the gas stream from the hot side elevates the surface temperature over the entire region. A liquid interior at $U_0^g = -1$ m s^{-1} is almost uniformly heated towards the symmetry axis. Correspondingly, large temperature gradients occur in the narrow region near the symmetry axis.

3.1.3. *Gas stream counter-directed with Marangoni force*

For liquids with $\partial\sigma/\partial T < 0$ the thermocapillary flow is always directed from the hot to the cold side at the interface. A gas at the mean temperature is moving against the Marangoni flow and causes competition between the action of shear and thermocapillary stresses. When a gas stream approaches the liquid zone near the cold corner, it faces the typical sharp maximum of the Marangoni velocity (as in figure 4*b*), which strongly resists the incoming gas flow. For small gas velocities the shear stress is too weak to blow away this peak. Because gas enters from the cold side and moves along the cold rod, its temperature approaches T_{cold} on the side of the liquid. Thus, the gas affects the liquid flow not only via shear stress but also by cooling the nearby interface and reducing the temperature gradient, driving the velocity peak. The flow topology depends on the gas speed.

The shear and thermocapillary stresses act to pull the interface apart and, finally, at $U_0^g = U_{0c}^g = 0.75$ m s^{-1} ($Re^g \approx 200$), a point with zero interface velocity appears around which the signs of the velocity are different. The temperature field and stream functions in this case are shown in figure 7. The flow pattern consists of two vortices with the opposite directions of the circulation where the vortex on the cold side is controlled by a gas flow and on the hot side by the Marangoni force. The gas velocity has a large effect on the further evolution of the flow pattern. At the gas speed just above U_{0c}^g the velocity on the whole interface is small, see curve 4 in figure 8(*a*), and the only limited region near the cold corner moves in the direction of the gas stream. With a small increase in the gas flow rate the shear stress takes control over half of the interface, see curve 5. The temperature gradient (figure 8*b*) has a peak near the cold wall and a more noticeable peak occurs at the stagnation point. The former peak widens with the gas speed while the latter one becomes sharper. Analysis of curves 5 and 6 gives a hint that the stagnation point on the interface plays the role of a 'cold'

https://doi.org/10.1017/jfm.2012.519 Published online by Cambridge University Press

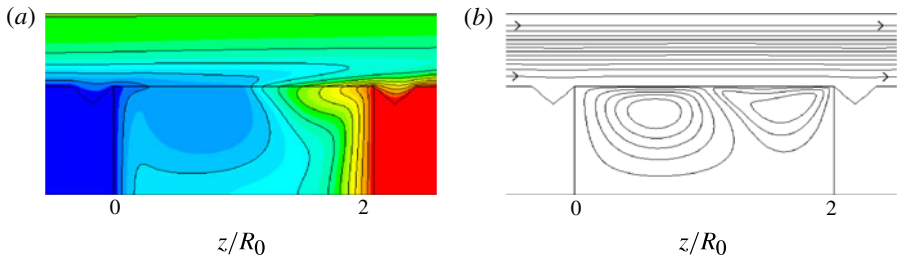


FIGURE 7. (Colour online) Isolines of temperature field and stream functions in two phases when $Pr = 68$, $\Delta T = 5$ K, $U_0^g = 1.0$ m s^{-1} ($Re^g = 273$) and $\Gamma = 2$.

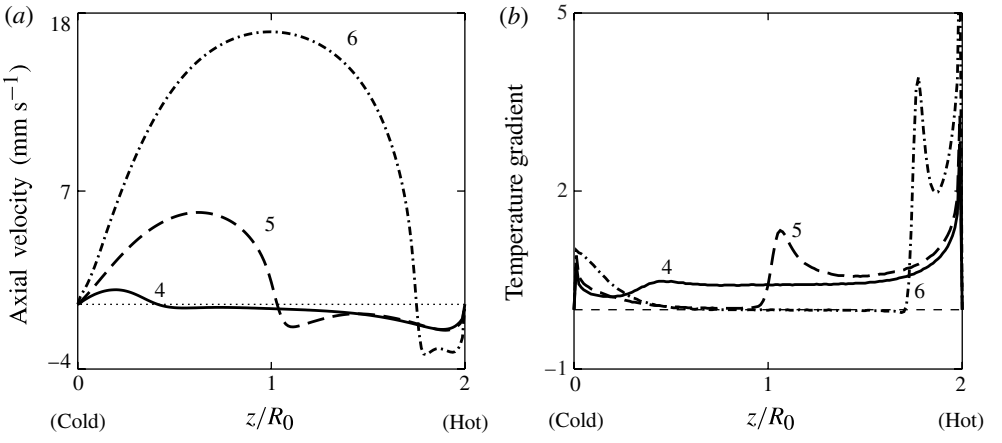


FIGURE 8. Axial velocity and dimensionless temperature gradient $(R/\Delta T)\partial_z T$ on the free surface when the flow is controlled by gas stream. Curves 4–6 correspond to $U_0^g = 0.75, 1, 2$ m s^{-1}, respectively. $Pr = 68$, $\Delta T = 5$ K and $\Gamma = 2$.

wall for the Marangoni-controlled region. A reduction of the Marangoni-controlled zone strengthens the flow inside.

The temperature profiles along and across the interface are shown in figure 9. For $U_0^g < \tilde{U}_{0c}^g$ the temperature on the free surface is a monotonically growing function as follows from curves 1–3 in figure 9(*a*). A sharp bend in the temperature profile occurs near the cold wall when the gas speed attains U_{0c}^g as shown by curve 4. It is a result of the appearance of two counter-rotating vortices instead of one. With a further increase in the gas speed the flat temperature profile is observed in the region controlled by the gas flow. The higher gas velocity provides an extension of the temperature plateau towards the hot wall.

The temperature profiles in the radial direction, shown in figure 9(*b*) at the mid-height $z = d/2$, are found to exhibit a non-trivial behaviour due to the existence of different flow regimes. The interior of the liquid as well as the gas phase are hottest in the cases of 'no gas' (the dashed curve) or zero speed gas (curve 1). Curves 2 and 3 display the cooling of the liquid in the bulk and, in particular, on the free surface. The maximum temperature in the liquid occurs beneath the free surface. Although the second vortex already appears at U_0^g corresponding to curve 4, its behaviour is similar

https://doi.org/10.1017/jfm.2012.519 Published online by Cambridge University Press

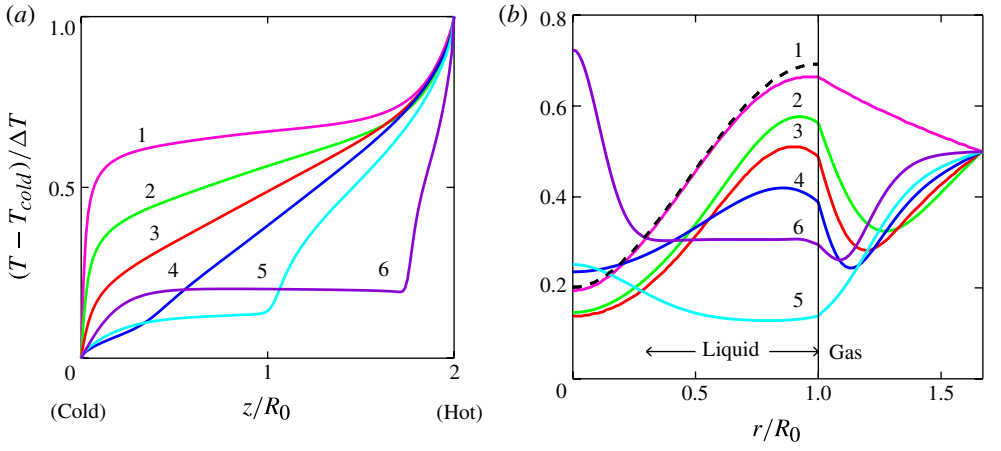


FIGURE 9. (Colour online) Temperature for different gas velocities (*a*) along and (*b*) across free surface in the middle of the liquid zone $z = d/2$. Curves 1–6 correspond to gas velocities $U_0^g = 0, 0.25, 0.5, 0.75, 1, 2$ m s^{-1} respectively. The dashed curve corresponds to the absence of a gas phase. Here $\Delta T = 5$ K, $T_0^g = T_{mean}$ and $\Gamma = 2$.

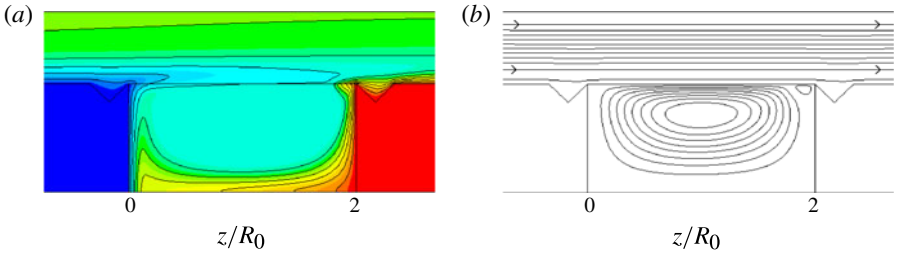


FIGURE 10. (Colour online) Isolines of the temperature field and stream functions in two phases when $Pr = 68$, $\Delta T = 5$ K, $U_0^g = 2.0$ m s^{-1} ($Re^g = 547$) and $\Gamma = 2$.

to curves 2 and 3 as the gas-controlled region of the flow does not reach the middle of the liquid zone. As soon as it happens, the temperature in the liquid sharply drops down (curve 5). The entire temperature field for this case is shown in figure 10(*b*). With a further increase of the gas speed the vortex near the hot side detaches from the wall and the small region, controlled by the Marangoni force, is located only near the interface. Consistently, the flow coming from the cold side reaches the hot side and liquid is heated up moving along the wall. By continuity the liquid moves out from the hot wall near the axis and the temperature in this region increases. The bulk temperature is colder and almost uniform. As a result curve 6 in figure 9(*b*) lies above the curve 5.

3.2. *Oscillatory instability*

3.2.1. *Non-steady flow regimes*

The regimes of heat/mass transfer described in the previous section for $Pr = 68$ were observed when $\Delta T \leqslant 5$ K. The values of the Marangoni number used in our simulations are below the critical value for the three-dimensional hydrothermal instability, $Ma_{cr} \sim 600 \cdot Pr \approx 4 \times 10^4$, reported by Lucasser (2011)

https://doi.org/10.1017/jfm.2012.519 Published online by Cambridge University Press

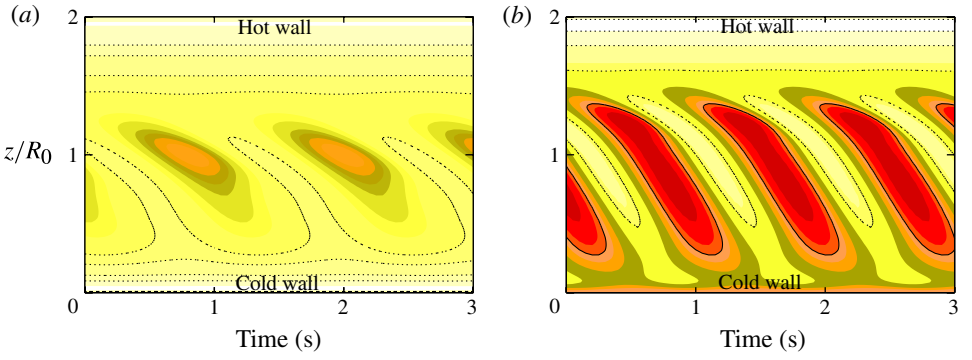


FIGURE 11. (Colour online) Convection cells on the interface as a projection of the interface velocity for $Pr = 68$, $Ma = 13\,700$ when (a) $Re^g = 240$ and (b) $Re^g = 410$. The dashed curves, given for better understanding, correspond to the negative velocity. The lighter colour corresponds to the stronger negative velocity. The solid line in graph (b) indicates zero velocity. The line levels are different in (a,b).

and Melnikov (2011) in the cases of motionless gas and a single-phase liquid bridge, correspondingly. Hereafter we consider another type of the oscillatory instability, which occurs at the lower values of Marangoni number, i.e. $Ma_{cr} = 9.1 \times 10^3$, $Re^g = 273$, $\Gamma = 2$ ($\Delta T_{cr} = 8$ K and $U_0^g = 1.0$ m s^{-1}). The dimensionless quantities Ma and Re^g will be used instead of ΔT and U_0^g for the description of an oscillatory instability which are recalculated as

$$Re^g = 273 U_0^g, \quad Ma_{Pr=68} = 573 \Gamma \Delta T, \quad Ma_{Pr=12} = 5572 \Gamma \Delta T. \tag{3.3}$$

In this subsection attention is focused on the development of oscillatory regimes and their features while the instability mechanism will be described in the next section. Two different regimes have been found depending on the gas velocity.

The first regime includes a few steps. Near the threshold of instability the Marangoni flow is sufficiently strong not only on the interface but also in the bulk and it does not allow the vortex with the opposite circulation to set in. Correspondingly, the interface velocity does not change sign in the course of oscillation, i.e. it remains negative. For better distinction of the regimes, figure 11(a) shows the time evolution of the interface velocity for the supercritical Marangoni number $Ma/Ma_{cr} = 1.5$ while Re^g corresponds to the threshold value and above. The stability diagram is given in figure 17. The flow intensity is outlined by colours: the stronger the velocity, the lighter the colour. A few dashed curves depict the flow behaviour in order to simplify understanding. The inclination of cells indicates that the disturbances propagate from the hot to the cold side. The oscillations of the velocity and temperature occur in the central part of the free surface because two pronounced peaks of the interface velocity near the hot and cold sides, caused by Marangoni force (see figure 4b), prevent the oscillations in these regions. Thus, in a wide area near the hot wall and a rather narrow region near the cold side the velocity remains constant with time, as shown by dotted horizontal curves.

At the next step, with increasing gas velocity from 0.85 to 1 m s^{-1} (Re^g from 240 to 273) at the same Marangoni number, e.g. $Ma = 13\,700$, a small recirculation zone is generated in the middle of the liquid being attached to the interface as shown in figure 12(a). The shear stress enables the birth of this small vortex by lowering the

https://doi.org/10.1017/jfm.2012.519 Published online by Cambridge University Press

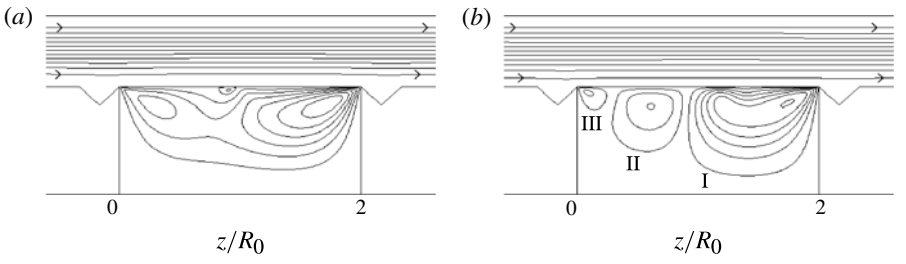


FIGURE 12. Snapshots of stream functions for different oscillatory regimes at $Pr = 68$, $Ma = 13\,700$, $\Gamma = 2$ when (*a*) $Re_0^g = 274$ and (*b*) $Re_0^g = 410$.

interface velocity and the thermocapillary stress forms the global circulation pattern. Note, that at this stage of the oscillatory regime the small vortex never penetrates deeply inside the liquid. The maxima of the amplitudes of velocity and temperature oscillations occur at the vortex location and gradually decrease towards the cold side and abruptly towards the hot side.

The vortex in the middle of the interface grows with the cold gas velocity, and at a certain time moment it reaches the symmetry axis and breaks the outermost streamlines of the global circulation pattern driven by Marangoni stresses as shown in figure 12(*b*). At that moment the flow pattern consists of three independent vortices and a small shadow of the fourth one near the interface. Two of them adjacent to the hot (I) and cold (III) walls rotate counterclockwise and the middle vortex (II) rotates clockwise. Note that the vortex near the cold wall still keeps the direction determined by the Marangoni force. Correspondingly, the scenario is as follows: the largest vortex (I) which occupies half of the free surface at the hot side, pushes the middle one to the cold side. In turn, the middle vortex (II) moves to the cold side compressing the nearby vortex (III) and leaving more space for the growing vortex (I). It faces a strong resistance of the vortex (III), which is in the region with high temperature gradients and despite its small size has a larger circulation. As a result vortex (II) loses energy, shrinks in size and, finally, disappears. Subsequently the dominating vortex (I) forms an elongated streamlines pattern occupying all of the liquid volume. At that time the flow pattern consists of two recirculation regions near the solid walls with the same direction of circulation embedded in a globally circulating flow, which is weak in the middle of the interface and gives a possibility for the birth of a new vortex with opposite rotation. The cycle is repeating (see supplementary movies for flow field Movie1_flow.avi and for temperature field Movie1_temp.avi, available at journals.cambridge.org/flm, when $Ma = 13\,700$ K and $Re^g = 340$). The size and shape of the convection cells in this oscillatory regime are correlated with the changes in the gas speed. Figure 11(*b*) exhibits smooth shapes of the convection cells where dashed curves are given for clarity of the picture and the solid curve corresponds to zero velocity. The magnitude of the positive velocity (dark region bounded by the solid curve) is quasi-uniform. Note that the cell with positive velocity does not reach the cold side. Towards the hot wall the velocity oscillations display a significant amplitude decrease and the amplitude tends to be very small at $z/R_0 > 1.6$. A twist in the cell's shape at $1.2 < z/R_0 < 1.4$ delimits the birth region of the recirculation cell.

The Second flow regime is found to exist with a further increase in gas speed. It is characterized by the formation of a vortex at the cold side with the direction of circulation opposite to that caused by the Marangoni force. This vortex

https://doi.org/10.1017/jfm.2012.519 Published online by Cambridge University Press

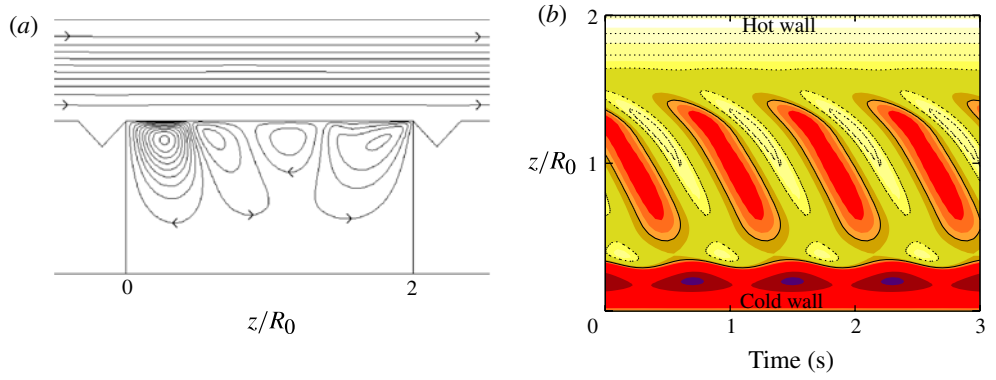


FIGURE 13. (Colour online) (*a*) Snapshots of stream functions and (*b*) convection cells on the interface as projection of the interface velocity. The lighter colour corresponds to the stronger negative velocity and the darker colour corresponds to the stronger positive velocity; $Re^g = 480$, $Ma = 13\,700$, $Pr = 68$ and $\Gamma = 2$.

exists permanently and indestructibly and the stagnation point, delimiting the vortex, performs only small displacements with time. The two vortices attached to the cold and hot walls control the flow. For a certain set of parameters, e.g. $Re^g = 480$ when $Ma = 13\,700$, they have comparable strengths but opposite rotations; hereafter, we call them 'basic' vortices. There exists a time instant when a flow pattern consists of a sequence of four counter-rotating vortices. Among them the two central ones are weaker than the side vortices, see figure 13(*a*). The basic vortices tend to destroy their weaker counter-rotating neighbours and push the pair of central vortices against each other. After destroying them the basic vortices stretch from one of the walls to the centre of the liquid zone. Alternatively, one of them occupies more than half of the liquid volume and becomes weak at its central part. It provides the possibility for the appearance of a new vortex near the interface which grows, reaches the symmetry axis and, consequently, breaks the original large vortex. As a result, the four-vortex flow state appears again. (See complementary movies for flow field Movie2_flow.avi and for temperature field Movie2_temp.avi when $Ma = 13\,700$ and $Re^g = 480$).

The convection cells for this regime are shown in figure 13(*b*). The solid curves correspond to zero velocity. The small elongated cells at the cold side outline the stable core of the vortex caused by the gas flow and the wavy horizontal curve depicts the location of the zero axial velocity. Accordingly, the uniform colours near the hot wall show the stable position of the vortex caused by the Marangoni flow. The large vertical cells correlate with the area of maximal vortex activity. With a further increase in the gas speed the vortex attached to the cold side expands drastically compressing the area where oscillations occur. The liquid temperature in the region occupied by the vortex becomes uniformly cold except a thin area near the symmetry axis, similar to figure 10(*a*). A vertical temperature gradient, needed for an instability to occur, is not sufficient and it exists only over a short region. The instability disappears and oscillations decay.

3.2.2. *Mechanism of instability*

An essential difference between the travelling wave described above and those obtained formerly in liquid bridges is in the direction of propagation. While the axisymmetric travelling wave found in a liquid bridge in the absence of a gas flow

https://doi.org/10.1017/jfm.2012.519 Published online by Cambridge University Press

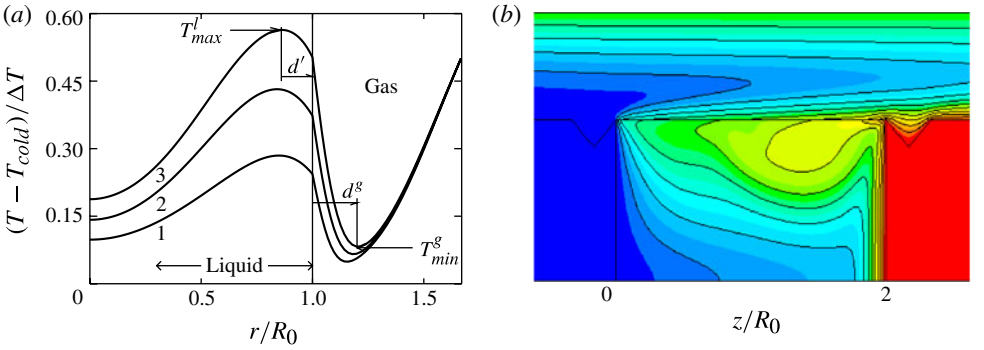


FIGURE 14. (Colour online) (*a*) Snapshots of radial temperature profiles at different axial positions. Curves 1–3 correspond $z/R_0 = 0.67, 1, 1.3$; $Re^g = 300$ $Ma = 9170$ and $\Gamma = 2$. (*b*) Snapshots of the temperature field at the oscillatory regime I $Re^g = 280$, $Ma = 11\,500$ and $\Gamma = 2$.

(Shevtsova, Melnikov & Nepomnyashchy 2009) moves from the cold end to the hot end, which is typical for hydrothermal waves, the wave observed in the presence of a cold gas flow moves to the cold end.

We attribute the unusual direction of the wave propagation to the inverted radial temperature distribution in the liquid near the interface, which is developed due to the cooling of the interface by the cold gas flow (see figures 14 and 15). The axial, $\partial_z T' = (R_0/\Delta T)\partial_z T$, and radial, $\partial_r T' = (R_0/\Delta T)\partial_r T$, temperature gradients in figure 15 are shown by the solid curves (1 and 2, respectively) while dashed curve shows dimensionless velocity on the free surface. The first three graphs, figure 15(*a–c*), correspond to the threshold value of the Marangoni number, i.e. $Ma_{cr} = 9100$, and to the Reynolds numbers: (*a*) below critical; (*b*) at the first oscillatory regime; and (*c*) at the second oscillatory regime. The radial component of the temperature gradient $\partial_r T'$ at the interface is negative, and it prevails over the axial component $\partial_z T'$ everywhere except the vicinity of the cold and hot ends. Recall that in the absence of the cooling gas the sign of $\partial_r T'$ at the interface is opposite. The temperature gradient inversion penetrates into the liquid on the distance which depends on the axial coordinate but typically is $\sim 0.2R_0$ (see snapshots of the temperature field in figure 14*a*). The temperature distribution in a liquid bridge near the interface cooled by gas is somewhat similar to that in a layer on a heated substrate, which is subject to the Pearson's instability (Pearson 1958). However, the thermocapillary flow created by the axial temperature gradient cannot be ignored by the consideration of the development of instability.

Let us consider a steady thermocapillary flow with $\partial_z T' > 0$ and $\partial_r T' < 0$, and impose a localized positive temperature disturbance on the interface around the point $z = z_0$. Such a disturbance will diminish the axial temperature gradient upstream of its location (at $z > z_0$) and enhance it downstream of its location (at $z < z_0$). That will lead to a decrease of the interfacial velocity at $z > z_0$ and its growth at $z < z_0$. Owing to the incompressibility of the liquid, a radial component of velocity will appear which will be negative in the region of the liquid deceleration and positive in the region of its acceleration. (In the region of the liquid deceleration, $\partial_z v_z < 0$, and from the continuity equation it follows that $\partial_r(rv_r) > 0$. Because $v_r = 0$ at the interface, $v_r < 0$ below the interface in the region of the deceleration.) Because $\partial_r T' < 0$, the radial flow will enhance temperature downstream of the disturbance and diminish it

https://doi.org/10.1017/jfm.2012.519 Published online by Cambridge University Press

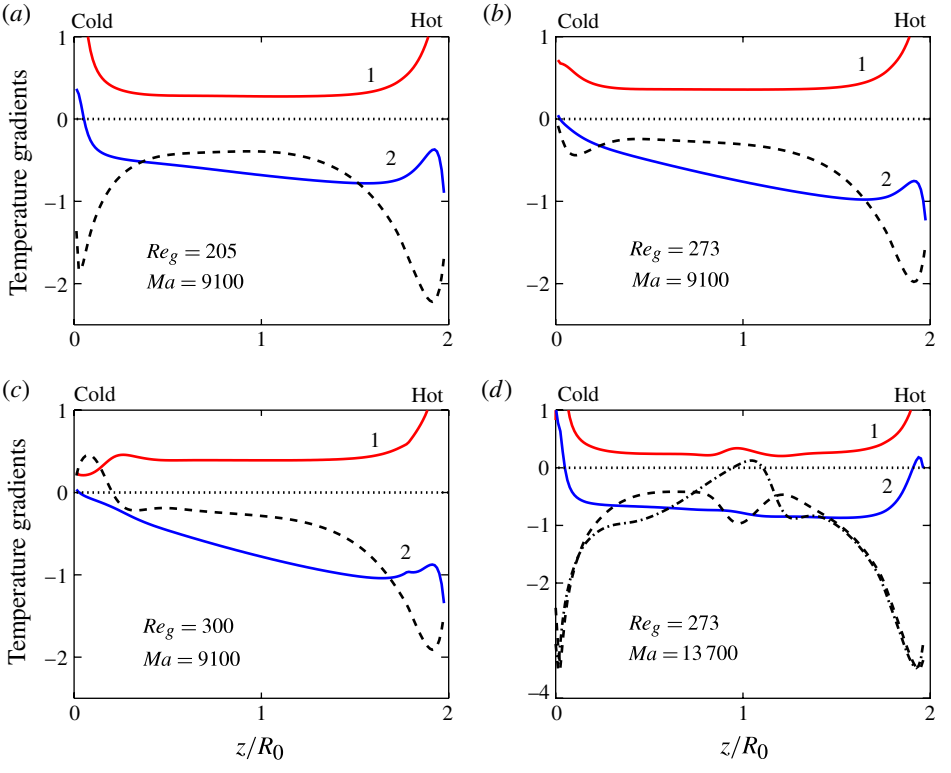


FIGURE 15. (Colour online) The axial, $\partial_z T'$, and radial, $\partial_r T'$, temperature gradients (solid curves 1 and 2) and dimensionless velocity $U/(\nu/R_0)$ on the free surface (dashed curve). Graphs (*a–c*) correspond to $Ma = 9100$ and $Re^g = 205$, 273 and 300, respectively. Graph (*d*) corresponds to $Ma = 13\,700$ and $Re^g = 273$ with two snapshots of the velocity.

upstream of the disturbance. Thus, the 'hot spot' will be shifted downstream, i.e. to the cold end. Another factor moving the temperature disturbance downstream, is the thermocapillary flow directed to the cold end. The mechanism of the amplification of the temperature disturbance is similar to that of the Pearson's instability. If the radial temperature gradient and the intensity of the flow are sufficiently large, the velocity disturbance created by the temperature disturbance brings to the interface an amount of hot liquid from a bulk sufficient for enhancement of the initial temperature disturbance. In that case an instability with respect to travelling waves moving to the cold end is developed, see a sketch in figure 16.

The deceleration of the flow due to the disturbance of the interfacial temperature distribution manifests itself in the appearance of a return interfacial flow and a vortex with opposite circulation (i.e. it provides an interface 'separation'). The boundary of the zero interfacial velocity is shown in figure 11 by solid line.

We have estimated the effective radial Marangoni number $Ma_\perp(z) = \sigma_T d^l(z)(T^l_{max} - T_{surf})/\mu^l\chi^l$, where $d^l(z)$ is the thickness of the region of the radial temperature inversion at a definite z, near the instability threshold. The maximum values of $Ma_\perp(z)$, which are between 39 and 44, are found in the interval $1.0 < z < 1.3$ where the travelling wave is apparently created. The observed critical value of the Marangoni number is lower than that of the Pearson's instability in a horizontal

https://doi.org/10.1017/jfm.2012.519 Published online by Cambridge University Press

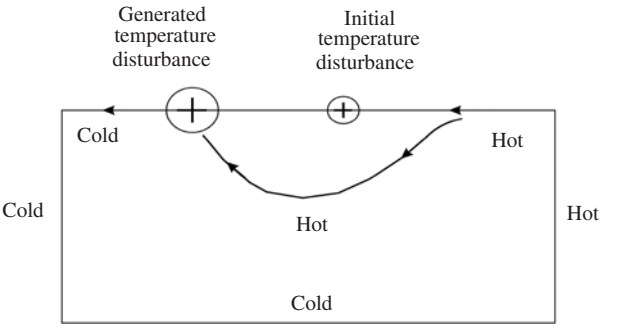


FIGURE 16. Sketch of the development of instability.

layer ($48 < Ma_{cr} < 80$, depending on the Biot number). The decrease of the critical Marangoni number as compared with the Bénard–Marangoni problem can be caused by the influence of the thermocapillary flow discussed above, and by the absence of a solid plate at the boundary of the inverted gradient region.

Note that an instability of a thermocapillary flow with respect to waves propagating downstream was found formerly in a horizontal layer in the presence of both longitudinal and transverse components of the temperature gradient, see Shklyaev & Nepomnyashchy (2004).

In the previous subsection an important role in the development of the perturbations was also assigned to the gas flow. There are three important contributions in flow organization: shear stress, cooling by gas (radial temperature gradient) and Marangoni flow (horizontal temperature gradient) and they are presented in figure 15. The axial temperature gradient at the steady case is smaller than at the oscillatory regimes $\partial_z T' \approx 0.28$ in the central part of figure 15(*a*) versus 0.35 and 0.39 in figure 15(*b,c*). The values of the radial gradient are not so different in the different regimes (figure 15*a–c*) just the slope of $\partial_r T'$ increases towards the hot wall with the increase of Re^g. The ratio of gradients, which is equal to ratio of radial and axial Marangoni numbers, $R_{Ma} = Ma_r/Ma_{ax} = \partial_r T/\partial_z T$ changes as [1.8–2.7] in steady regimes and as [1.16–2.5] in the oscillatory regime when $0.5 < z < 1.5$. Because the ratio R_{Ma} is larger in the steady regime than in the oscillatory regime, the new instability cannot be explained using an approach of inclined temperature gradient in the layer as in the papers by Nepomnyashchy, Simanovskii & Braverman (2001) and Ueno, Kurosawa & Kawamura (2001). In addition, the interface velocity undergoes sizeable modifications with the increase of the shear stress. Its peak value at the cold side is considerably smaller at $Re^g = 275$, figure 15(*b*), than in the steady regime when $Re^g = 205$, figure 15(*a*). A comparison of figure 15(*a,b*) shows that the velocity on the interface in the region $0.5 < z < 1$ decreases by about $\approx 30\%$ due to the increase of the shear stress. This drop of the velocity enables the birth of the small vortex at the central part of the interface and progress of the oscillatory regime.

A comparison of figure 15(*b,d*) may shed light on the role of *Ma* as these graphs corresponds to the same $Re^g = 273$ but *Ma* differs by 50 %, i.e. $Ma = 9100$ and 13 700. Both graphs present the flow in the first oscillatory regime. Two snapshots of axial velocity indicate at the large amplitude of the oscillations. The flow in general is more intense for larger *Ma* number (scales on vertical axes are different) and the radial temperature gradient is uniformly large over the entire free surface.

https://doi.org/10.1017/jfm.2012.519 Published online by Cambridge University Press

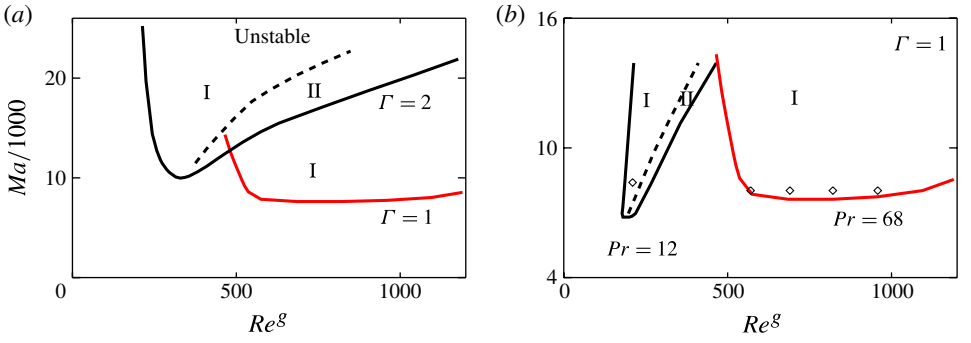


FIGURE 17. (Colour online) Stability diagram (Ma versus Re^g) for (a) silicone oil ($Pr = 68$) at two different aspect ratios $\Gamma = 1, 2$; (b) for n-decane ($Pr = 12$) and silicone oil ($Pr = 68$) for the aspect ratio $\Gamma = 1$ Remember that $Re^g = 273U_0^g$, $Ma_{Pr=68} = 573\Gamma\Delta T$ and $Ma_{Pr=12} = 5572\Gamma\Delta T$.

3.2.3. *Stability boundaries*

The oscillatory regimes described above are summarized in the stability diagrams in figure 17. An instability occurs inside the regions limited by the solid curves. The dashed curves depict the boundary between two oscillatory regimes when the first (I) is controlled by the Marangoni force (figure 12) and second (II) is controlled by the shear stress (figure 13). Figure 17(a) presents the stability diagrams (Ma versus Re_0^g) for $Pr = 68$ at two different aspect ratios. For the longer interface ($\Gamma = 2$) the instability curve has a clear minimum and its left branch is almost a vertical line. The critical speed of the gas (and, hence, the shear stress) change only by $\sim$20 % when Ma (or ΔT) increases by 2.5 times. The right branch of the stability diagram, corresponding to the decay of oscillations, exhibits almost linear growth with Re^g. For the shorter bridges ($\Gamma = 1$) the instability sets in at larger gas velocity and beyond the threshold value of Re_{cr}^g the critical Marangoni number remains almost constant with the increase of the gas velocity. Because the action of the shear stress develops on the small length of the free surface the second regime of instability (dominated by shear stress) is not observed in this case.

Figure 17(b) shows the stability curves for liquids with $Pr = 12$ and $Pr = 68$ for unit aspect ratio. It helps to understand the tendency observed with variation of the viscosity of the liquid because the thermal diffusivity of liquids differs by $\sim$10 % and its effect could be not so important. A change in Prandtl number results in a significant shift in the position of the minimum indicating the important role of the shear stress. Decreasing Pr by $\sim$6 times essentially shifts stability curve to the lower gas velocities, i.e. from $Re_{cr}^g = 570$ (silicone oil) to $Re_{cr}^g = 208$ (n-decane) while the critical Ma decreases by $\sim$10 %. The increase of the shear stress enables existence of the second oscillatory regime but diminishes the horizontal extension of the instability region. For example, at $Ma \approx 8000$ (depicted by symbols in figure 17b) the region of instability in the plane of Reynolds number is $\sim$7 times narrower for $Pr = 12$ than for $Pr = 68$. It occurs because the larger shear stress easier suppresses the peak of the interface velocity near cold wall and facilitates setting and expansion of the vortex near the cold side with rotation opposite to the Marangoni flow.

As mentioned above, the thermal effects play an important role in the development of instability. Figure 18(a) demonstrates the effect of the gas temperature on the development of the oscillations. All of the curves show the temporal evolution of the

https://doi.org/10.1017/jfm.2012.519 Published online by Cambridge University Press

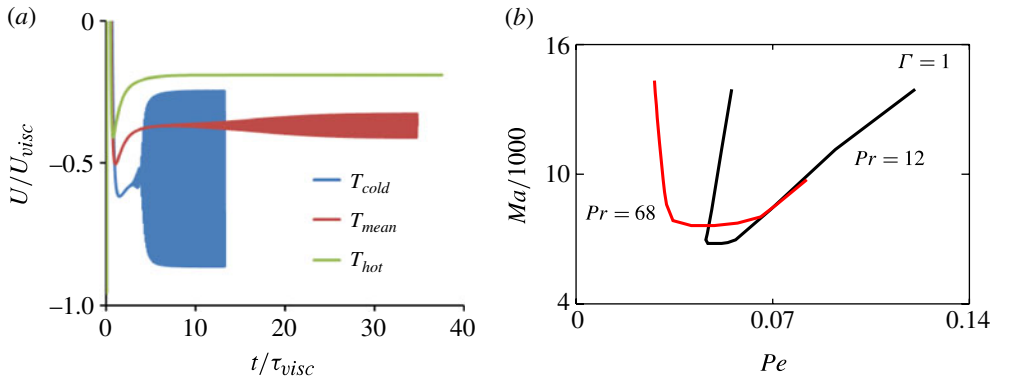


FIGURE 18. (Colour online) (*a*) Amplitude of the liquid velocity oscillations for different temperatures of the inlet gas at the point $z/R_0 = 1$, $r/R_0 = 0.83$ when $Re^g = 274$, $Ma = 6900$, $Pr = 68$ and $\Gamma = 2$. (*b*) Stability diagram as a function of the Péclet number $Pe = U_0^g(\mu^g/\mu^l)R_0/\chi^l$ (plot of Ma versus Pe).

velocity at the interface in the point $z/R_0 = 1$, $r/R_0 = 0.83$ in time for $Ma = 6900$ and $Re_0^g = 274$ when the gas enters from the cold side but at different inlet temperatures. The gas temperature strongly affects the development of the sustained oscillations in time and their amplitude. The characteristic viscous time $\tau_{vis} = d^2/\nu = 7.2$ s and velocity ($U_{vis} = \nu/d$) are used as scales in figure 18(*a*) (the thermal time is $\tau_{th} = Pr\,\tau_{vis}$). In the case when the gas temperature is equal to that of the hot wall the amplitude of oscillations is tiny and needs time longer than $40\tau_{vis}$ to reach its steady value. When the gas temperature is equal to the mean temperature, the amplitude of oscillations is well visible in figure 18(*a*) and the development of the sustained oscillations needs $\sim 30\tau_{vis}$. In the case of cold gas the development of the instability takes only 5–6τ_{vis} and the amplitude is more than three time larger than in the case of a mean temperature. An intense development of the oscillations with the decrease of the gas temperature indicates that the thermal effects and, in particular, the gas temperature are important for the mechanism of oscillations.

The hydrodynamics of the resulting flow in liquid exhibits sensitive dependence on the shear stress, interfacial thermal condition and on the fluid properties. Correspondingly, the Péclet number ($Pe = R_0U^l/\chi^l$) could be an appropriate quantity to characterize the stability of the system. For the calculation of Péclet number the liquid velocity can be evaluated via gas velocity from (3.2), $U^l \sim U_0^g/\tilde{\mu}$. The stability curves in figure 18(*b*) presenting Ma as a function of a modified Péclet number $Pe = U_0^g R_0/(\tilde{\mu}\chi^l)$ indicate that instability islands for $Pr = 12$ and $Pr = 68$ strongly overlap. Indeed, the Péclet number which expresses the relative contribution of advective to thermal diffusive transport mechanisms is suitable quantity for analysis of the instability in this problem. One can observe from the scaling of the axis in figure 18(*b*) that instability occurs at a Péclet number much smaller than unity, indicating that thermal motion prevails over the mass transport.

Let us discuss now the dependence of the oscillation frequency on the parameters Ma, Pr, Re_0^g and Γ (see figure 19). First of all, the effect of Ma on the frequency is almost negligible. At the same time, the dependence of the non-dimensional frequency (scaled with ν/d^2) on Pr is significant (figure 19*a*). Note that dimensional frequencies are of the same order, ~2–4 Hz, for both liquids. The frequency grows with Re_0^g

https://doi.org/10.1017/jfm.2012.519 Published online by Cambridge University Press

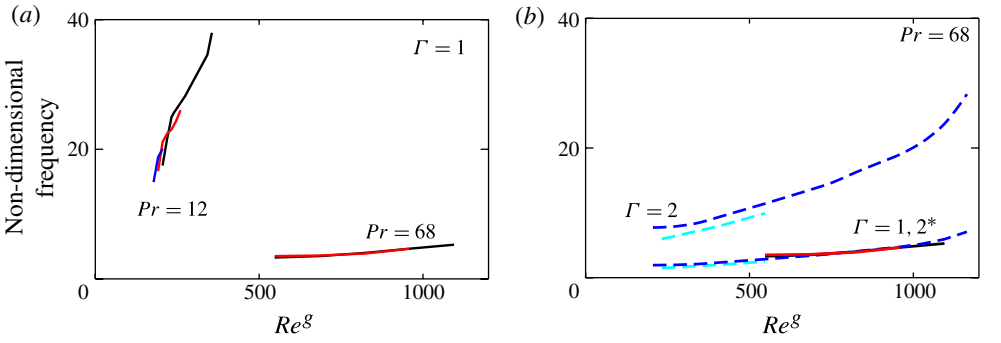


FIGURE 19. (Colour online) Frequency of oscillations scaled as $f_{ch} = \nu/d^2$ for: (*a*) aspect ratio $\Gamma = 1$ when $Pr = 12$ (three curves correspond to $Ma = 7000$, 8400 and 11 150 according to their length) and $Pr = 68$ (two superimposed curves at $Ma = 8000$ and $Ma = 8600$ distinguished by colours); and (*b*) two different aspect ratios $\Gamma = 1$ and 2 for ($Pr = 68$). Notation $\Gamma = 2^*$ means the different scaling $f_{ch} = \nu/R_0^2$.

(see figure 19); this growth is especially strong for the liquid with a lower viscosity ($Pr = 12$). The change of the curve slope at the points of the transitions between regimes is weak for $Pr = 12$ and negligible for $Pr = 68$.

The effect of aspect ratio Γ on frequency is examined in figure 19(*b*) which includes two data sets for $Pr = 68$. The two dashed curves in the upper part of the graph show a gradual increase of the frequency with Re_0^g for an aspect ratio of $\Gamma = 2$. The solid curves in the bottom part correspond to $\Gamma = 1$. It is interesting to note that using a different scaling of frequency with radius of the liquid bridge (ν/R_0^2) instead of its length leads to a coincidence of curves with different Γ. This gives a hint that the heat mass transfer in the radial direction is responsible for the oscillatory instability.

3.2.4. *Heat flux*

Another important effect to analyse is the heat flux (Biot number) through the interface, which is needed for theoretical and numerical analysis in a single-phase flow formulation. It was presented above in figure 4(*a*) that in the case of zero gas velocity, the heat transfer rate is relatively uniform over a large part of the surface with a small region of large heat loss near the solid walls. The heat loss ($q > 0$) is increased approaching the onset of the instability. Figure 20(*a*) illustrates that at the threshold of instability the uniformity of the heat flux declines and the heat loss near the hot wall is larger than near the cold side. Although the heat loss in general is smaller for $Pr = 12$ than for $Pr = 68$ at the similar Marangoni numbers ($Ma \sim 8000$) the heat flux values for $Pr = 12$ display a sharp increasing trend towards hot wall. A larger shear stress provides a stronger increase of heat loss in the direction of gas flow. Two snapshots in time for each Pr number presented in figure 20(*a*) elucidate that in the case of large viscosity contrast, $\tilde{\mu} = 250$ ($Pr = 68$), the oscillations occur in the central part of the interface while for smaller viscosity contrast, $\tilde{\mu} = 42$ ($Pr = 12$), they occupy almost all of the free surface.

Figure 20(*b*) illustrates the redistribution of the heat loss along the free surface with the increase of gas velocity. Curves 1–4 (snapshots) correspond to successive increase of Reynolds number, $Re^g = 560$, 685, 820 and 960 at the same Marangoni number and aspect ratio. The positions of these curves on the stability diagram are depicted by symbols in figure 17(*b*). The total effect is associated with the behaviour of the radial

https://doi.org/10.1017/jfm.2012.519 Published online by Cambridge University Press

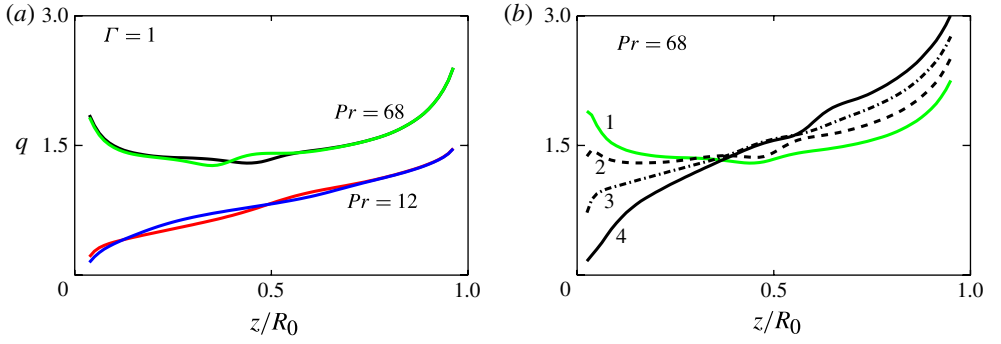


FIGURE 20. (Colour online) Distribution of heat flux along the free surface for $\Gamma = 1$; (*a*) snapshots for $Pr = 12$, $Ma = 8400$ and $Pr = 68$, $Ma = 8000$; (*b*) evolution of heat flux profile with Re^g when $Ma = 8000$. Curves 1–4 correspond to $Re^g = 560$, 685, 820 and 960, respectively.

temperature gradient. The change in Reynolds number results in a significant decrease of the heat flux on the cold side and increase at the hot side. The lowering of the heat flux values on the cold side is stronger than growth on the hot side.

4. Conclusions

In the present work, we have performed an extensive computational study on the effects of the ambient air flow on a thermocapillary convection in high-Prandtl-number liquids: $Pr = 12$ (*n*-decane) and $Pr = 68$ (5 cSt silicone oil). The mathematical model assumed incompressibility of the liquid and gas, linear dependence of the surface tension on temperature, with all other thermophysical properties of the fluids being taken as constant. The geometry of the physical problem is a cylindrical and non-deformable liquid bridge concentrically surrounded by an annular gas channel under conditions of zero gravity. The inlet velocity and temperature of the gas are the control parameters as well as the temperature difference between end rods of the liquid bridge. The investigations were focused on axisymmetric solutions in the case of large gas speeds and small duct size.

When the liquid bridge is surrounded by a passive gas with a mean temperature, which is typical for the experiments, the free surface becomes colder in comparison with the no-gas case. In addition, the heat loss makes the thermocapillary driving force important over a larger part of the free surface compared with the insulated case. In general, the heat loss enhances the flow at the interface while the heat gain slows down the flow.

The forced gas flow along the interface provides two actions: via shear stresses and heat exchange. The steady flow was examined for the mean gas temperature at the inlet. In the case of a gas stream co-directed with the Marangoni flow, at very low gas velocity the flow in the liquid slows down because of the heat gain and for larger gas velocity the flow speeds up as viscous shear stress tends to pull the liquid along with it and accelerates the flow. When the gas stream is counter-directed with respect to the Marangoni flow, the flow pattern is drastically affected by the gas velocity. The shear and thermocapillary stresses act to tear the interface apart and the interfacial flow separation happens at certain gas speed.

https://doi.org/10.1017/jfm.2012.519 Published online by Cambridge University Press

We have found a new oscillatory instability at the critical values of the couple $[\Delta T_{cr}, U^g_{0cr}]$ when the gas is blown from the cold side. We assign the appearance of the instability to cooling the interface by the gas with additional action of counter directed shear stresses which decelerate the velocity of the free surface. Apparently the thermal effect of the gas is more important than the shear stress provided by the gas. In our opinion the suitable parameter for analysis of the instability is the Péclet number, $Pe = U^g_0(\mu^g/\mu^l)R_0/\chi^l$, which expresses the relative contribution of advective to thermal diffusive transport. In the region where instability occurs Pe is much smaller than unity. The stability diagram as a function (Ma versus Re^g_0) displays a limited region of the parameter space where the instability occurs. Attention is paid to the influence of the Prandtl number and aspect ratio on the instability islands. Two different regimes of instability are identified inside this parameter space.

The travelling wave in the presence of a cold gas flow propagates from the hot to cold end. The mechanism of this new instability is similar to the case of a return flow in the horizontal layer, although the direction of the travelling wave is opposite. We attribute the unusual direction of the wave propagation to the inverted radial temperature distribution in the liquid near the interface, which is developed due to the cooling of the interface by the cold gas flow.

The instability evolves under the action of three effects: the shear stress diminishing the interface velocity, the radial velocity disturbance tending to shift the temperature disturbance downward and the plain drift of the disturbance by the net thermocapillary flow. Some similarity can be found with the problem by considering an inclined temperature gradient in the liquid layer of a water–air system (Nepomnyashchy *et al.* 2001). The authors found that Pearson's instability (longitudinal convective rolls) exists in a bounded interval of Marangoni numbers and when the vertical temperature gradient 2.7 times larger than the horizontal one. In the present case the instability was observed when the mean value of the Marangoni ratio over active part of the interface is about $R_{Ma} \approx 2.2$ and above. By the order of magnitude the values of R_{Ma} are comparable.

The configuration of the most relevant experimental works (Ueno *et al.* 2010; Yano *et al.* 2012) do not allow us to observe this instability. The discovered gas-generated oscillatory instability may have implications for the approach of stabilization based on using an adjacent gas flow and it is expected to be studied in the course of the JEREMI experiment.

Acknowledgement

This work is supported by the PRODEX programme of the Belgian Federal Science Policy Office and ESA.

Supplementary movies

Supplementary movies are available at journals.cambridge.org/flm.

REFERENCES

DAVIS, S. H. 1987 Thermocapillary instabilities. *Annu. Rev. Fluid Mech.* **19**, 489.

GAPONENKO, YU., RYZHKOV, I. & SHEVTSOVA, V. 2010 On flows driven by mechanical stresses in a two-phase system. *Fluid Dyn. Mater. Process.* **6**, 1–75.

GAPONENKO, YU., MIALDUN, A. & SHEVTSOVA, V. 2011 Liquid entrainment by gas flow along the interface of a liquid bridge. *Eur. Phys. J. Special Topics* **192**, 63.

https://doi.org/10.1017/jfm.2012.519 Published online by Cambridge University Press

GAPONENKO, YU., MIALDUN, A. & SHEVTSOVA, V. 2012 Interfacial shear stress in gas–liquid flow in annuli. *Intl J. Multiphase Flow* **39**, 205.

HERRADA, M. A., LOPEZ-HERRERA, J. M., VEGA, E. J. & MONTANERO, J. M. 2011 Numerical simulation of a liquid bridge in a coaxial gas flow. *Phys. Fluids* **23**, 012101.

IRIKIRA, M., ARAKAWA, Y., UENO, I. & KAWAMURA, H. 2005 Effect of ambient fluid flow upon onset of oscillatory thermocapillary convection in half-zone liquid bridge. *Microgravity Sci. Technol.* **16**, 174.

KAMOTANI, Y., WANG, L., HATTA, L., WANG, A. & YODA, S. 2003 Free surface heat loss effect on oscillatory thermocapillary flow in liquid bridges of high Prandtl number fluid. *Intl J. Heat Mass Transfer* **46**, 3211.

KAWAMURA, H., TAGAYA, E. & HOSHINO, Y. 2007 A consideration on the relation between the oscillatory thermocapillary flow in a liquid bridge and the hydrothermal wave in a thin liquid layer. *Intl J. Heat Mass Transfer* **50**, 1263.

KUHLMANN, H. C. 1999 *Thermocapillary Convection in Models of Crystal Growth*. Springer.

LAPPA, M. 2010 *Thermal Convection: Pattern, Evolution and Stability*. John Wiley & Sons.

LAPPA, M., SAVINO, R. & MONTI, R. 2001 Three-dimensional numerical simulation of Marangoni instabilities in liquid bridges: influence of geometrical aspect ratio. *Intl J. Numer. Meth. Fluids* **36**, 53.

LOMBARDI, P., DE ANGELOS, V. & BANERJEE, S. 1986 Direct numerical simulation of near-interface turbulance in coupled gas–liquid flow. *Phys. Fluids* **8** (6), 1643.

LUCASSER, M. 2011 Thermocapillary convection in a liquid bridge influenced by an ambient gas; linear stability boundaries. Presentation at the JEREMI project meeting, Tsukuba, Japan.

MASUD, J., KAMOTANI, Y. & OSTRACH, S. 1997 Oscillatory thermocapillary flow in cylindrical columns of high Prandtl number fluids. *J. Thermophys. Heat Transfer* **11** (1), 105.

MATSUNAGA, T., MIALDUN, A., NISHINO, K. & SHEVTSOVA, V. 2012 Measurements of gas/oil free surface deformation caused by parallel gas flow. *Phys. Fluids* **24**, 062101.

MELNIKOV, D. 2011 Accumulation of particles in periodic flows. Presentation at the JEREMI project meeting, Tsukuba, Japan.

MIALDUN, A. & SHEVTSOVA, V. 2006 Influence of interfacial heat exchange on the flow organization in liquid bridge. *Microgravity Sci. Technol.* **18**, 146.

MONTANERO, J. M., FERRERA, C. & SHEVTSOVA, V. 2008 Experimental study of the free surface deformation due to thermal convection in liquid bridges. *Exp. Fluids* **45**, 1087.

NEPOMNYASHCHY, A. A., SIMANOVSKII, I. B. & BRAVERMAN, L. M. 2001 Stability of thermocapillary flows with inclined temperature gradient. *J. Fluid Mech.* **442**, 141.

PEARSON, J. R. A. 1958 On convection cells induced by surface tension. *J. Fluid Mech.* **4**, 489.

RYZHKOV, I. I. & SHEVTSOVA, V. 2012 Thermocapillary instabilities in liquid columns under co- and counter-current gas. *Intl J. Heat Mass Transfer* **55**, 1236–1245.

SHEVTSOVA, V. M., NEPOMNYASHCHY, A. A. & LEGROS, J. C. 2003 Thermocapillary-buoyancy convection in a shallow cavity heated from the side. *Phys. Rev.* E **67**, 066308.

SHEVTSOVA, V. 2005 Thermal convection in liquid bridges with curved free surfaces: benchmark of numerical solutions. *J. Cryst. Growth* **280**, 632–651.

SHEVTSOVA, V., MIALDUN, A. & MOJAHED, M. 2005 A study of heat transfer from liquid bridge interfaces to surroundings. *J. Non-Equilib. Thermodyn.* **30**, 261.

SHEVTSOVA, V., MIALDUN, A., FERRERA, C., ERMAKOV, M., CABEZAS, M. G. & MONTANERO, J. M. 2008 Subcritical and oscillatory dynamic surface deformations in non-cylindrical liquid bridges. *Fluid Dyn. Mater. Process.* **4**, 43.

SHEVTSOVA, V., MELNIKOV, D. E. & NEPOMNYASHCHY, A. 2009 New flow regimes generated by mode coupling in buoyant-thermocapillary convection. *Phys. Rev. Lett.* **102**, 134503.

SHEVTSOVA, V., MIALDUN, A., KAWAMURA, H., UENO, I., NISHINO, K. & LAPPA, M. 2011 Onset of hydrothermal instability in liquid bridge. Experimental benchmark. *Fluid Dyn. Mater. Process.* **7**, 1.

SHKLYAEV, O. E. & NEPOMNYASHCHY, A. A. 2004 Thermocapillary flow under an inclined temperature gradient. *J. Fluid Mech.* **504**, 99.

https://doi.org/10.1017/jfm.2012.519 Published online by Cambridge University Press

SIMIC-STEFANI, S., KAWAJI, M. & YODA, S. 2006 Onset of oscillatory thermocapillary convection in acetone liquid bridges: the effect of evaporation. *Intl J. Heat Mass Transfer* **49**, 3167.

SMITH, M. K. & DAVIS, S. H. 1983 Instabilities of dynamic thermocapillary liquid layers. Part 1. Convective instabilities. *J. Fluid Mech.* **132**, 119.

SMITH, M. K. 1986 Instability mechanisms in dynamic thermocapillary liquid layers. *Phys. Fluids* **29**, 3182.

TIWARI, S. & NISHINO, K. 2007 Numerical study to investigate the effect of partition block and ambient air temperature on interfacial heat transfer in liquid bridges of high Prandtl number fluid. *J. Cryst. Growth* **300**, 486.

TIWARI, S. & NISHINO, K. 2010 Effect of confined and heated ambient air on onset of instability in liquid bridges of high *Pr* fluids. *Fluid Dyn. Mater. Process.* **6**, 1–109.

UENO, I., KUROSAWA, T. & KAWAMURA, H. 2001 Thermocapillary convection in thin liquid layer with temperature gradient inclined to free surface. In *Heat Transfer 2002, Proceedings of Twelfth International Heat Transfer Conference*, pp. 129–133. Elsevier.

UENO, I., KAWAZOE, A. & ENOMOTO, H. 2010 Effect of ambient-gas forced flow on oscillatory thermocapillary convection of half-zone liquid bridge. *Fluid Dyn. Mater. Process.* **6**, 1–99.

WANG, A., KAMOTANI, Y. & YODA, S. 2007 Oscillatory thermocapillary flow in liquid bridges of high Prandtl number fluid with free surface heat gain. *Intl J. Heat Mass Transfer* **50**, 4195.

XU, J.-J. & DAVIS, S. H. 1984 Convective thermocapillary instabilities in liquid bridges. *Phys. Fluids* **27**, 1102.

YANO, T., NISHINO, K., KAWAMURA, H., UENO, I., MATSUMOTO, S., OHNISHI, M. & SAKURAI, M. 2012 3-D PTV measurement of Marangoni convection in liquid bridge in space experiment. *Exp. Fluids* **53**, 9.

https://doi.org/10.1017/jfm.2012.519 Published online by Cambridge University Press